Earth and Planetary Science Letters 592 (2022) 117609

Contents lists available at ScienceDirect

Earth and Planetary Science Letters

www.elsevier.com/locate/epsl

Jurassic true polar wander recorded by the Lhasa terrane on its northward journey from Gondwana to Eurasia

Zhenyu Li [a,b,*], Lin Ding [a,b,c], Douwe J.J. van Hinsbergen [d], Peter C. Lippert [e], Yahui Yue [a,b], Jing Xie [a,b], Yaofei Chen [f], Xudong Guo [a,c], Dingding Zhang [a], Tengge Zhao [a,c], Bailing Wu [g], Hangjun Li [a,h], Songlin He [a,c]

[a] State Key Laboratory of Tibetan Plateau Earth System, Resources and Environment (TPESRE), Institute of Tibetan Plateau Research, Chinese Academy of Sciences, Beijing 100101, China
[b] Center for Excellence in Tibetan Plateau Earth Sciences, Chinese Academy of Sciences, Beijing 100101, China
[c] University of Chinese Academy of Sciences (UCAS), Beijing 100049, China
[d] Department of Earth Sciences, Utrecht University, Princetonlaan 8A, 3584 CB Utrecht, the Netherlands
[e] Department of Geology and Geophysics, The University of Utah, Salt Lake City, 84112, UT, USA
[f] Institute of Science and Technology Strategy, Jiangxi Academy of Sciences, Nanchang 330029, China
[g] Institute of Geomechanics, Chinese Academy of Geological Sciences, Beijing 100081, China
[h] College of Engineering and Technology, Tibet University, Lhasa 850000, China

ARTICLE INFO

Article history:
Received 14 December 2021
Received in revised form 18 April 2022
Accepted 11 May 2022
Available online xxxx
Editor: A. Webb

Keywords:
Lhasa terrane
trench migration rates
true polar wander
paleolatitude
paleomagnetism
late Jurassic

ABSTRACT

Paleomagnetic data constrain paleogeographic motion of rocks relative to the Earth's spin axis, which is a sum of plate motion relative to the mantle and true polar wander. Discerning between these effects is challenging for studies aiming to reconstruct paleo-plate motions from deformed orogenic terranes. Here, we study the paleolatitudinal drift history of the Lhasa terrane of southern Tibet that migrated from the northern Gondwana to the southern Eurasian margin between late Triassic and early Cretaceous time. Previous work identified a 180 Ma near-equatorial Lhasa latitude and assumed near-constant paleolatitudinal drift. Large-scale true polar wander at this time, however, which has been argued for in previous work, requires highly variable Lhasa plate motion rates relative to Gondwana. Here, we test whether the alternative interpretation of constant plate motion rates provides a better prediction of paleomagnetic data. To this end, we present a new paleomagnetic pole from ~155 Ma volcanics (here dated by U/Pb zircon) of the Lhasa terrane. Our pole comprises site mean directions from 46 lavas, passes a fold test, and is supported by an extensive rock magnetic and microscopic analysis that reveals no evidence of remagnetization. Our results give an average direction of $D \pm \Delta D_x = 337.1° \pm 2.6°$, $I \pm \Delta I_x = -13.8° \pm 4.9°$, and a corresponding paleopole position at $\lambda_p = 45.3°$N, $\varphi_p = 295.3°$E with K=69.8 and $A_{95} = 2.5°$, predicting a similar near-equatorial, paleolatitude as at 180 Ma. This paleolatitudinal standstill is consistent with predicted paleolatitudes from global APWPs that account for Jurassic TPW and assume a constant Lhasa-Gondwana (India) oceanic spreading rate of ~8 cm/a during the 215-130 Ma opening of the Neotethys and closure of the Mesotethys oceans. Contemporaneous arc magmatism on the Lhasa terrane was previously interpreted to indicate that the Lhasa terrane was located above a subduction zone during its northward journey to Tibet: our results show that if our reconstruction is accurate, then trench migration rates also must have been ~8 cm/a. Our results are consistent with the range of rates of global long-lived trench migration that have been reconstructed in other studies, but they are much higher than measured in most modern systems. Our results more completely document the Lhasa terrane's separation from Gondwana and provide a straightforward methodology of using paleomagnetic data to test plate kinematic scenarios, overcoming the problem of the unknown effect of true polar wander on paleomagnetic data from deformed terranes.

1. Introduction

Paleomagnetism provides the sole quantitative tool for reconstructing the position of rocks, and the plates they formed on,

* Corresponding author at: State Key Laboratory of Tibetan Plateau Earth System, Resources and Environment (TPESRE), Institute of Tibetan Plateau Research, Chinese Academy of Sciences, Beijing 100101, China.
E-mail address: lizy@itpcas.ac.cn (Z. Li).

https://doi.org/10.1016/j.epsl.2022.117609
0012-821X/

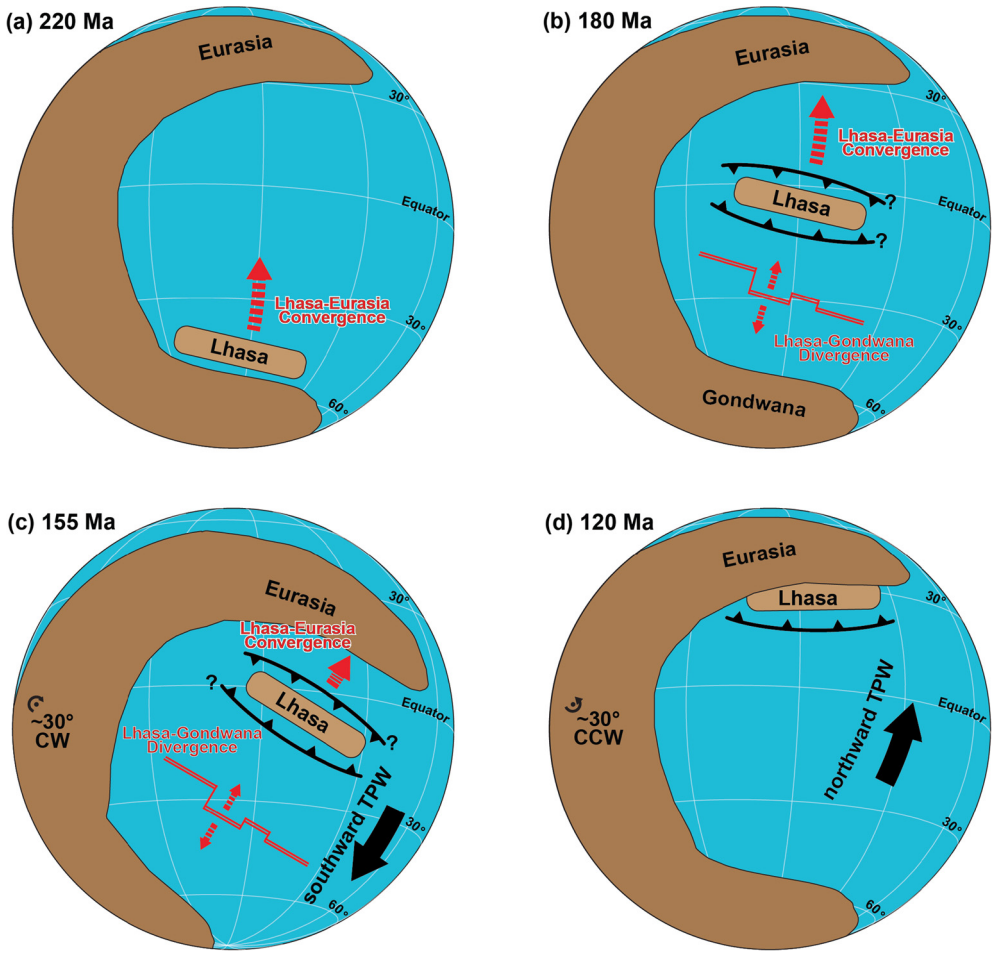

Fig. 1. Cartoon showing the combined effect of northward motion of a tectonic terrane and south-directed true polar wander (TPW). TPW occurs by ∼30° clockwise about a pole of rotation located at equatorial latitudes and low easterly longitude, followed by a similar magnitude of counterclockwise rotation about the same pole a few million years later. The superposition of northward plate motion and southward TPW produces an apparent paleolatitude standstill that would be resolved by paleomagnetic data from the terrane.

relative to the geodynamo that on geological timescales aligns with the Earth's spin axis (e.g., Torsvik et al., 2012). Paleomagnetic data from all plates that are tied together in a plate circuit may be rotated into the coordinates of a single reference plate and combined into global apparent polar wander paths (GAPWaPs) (e.g., Besse and Courtillot, 2002; Torsvik et al., 2012) that provide the reference frame to constrain paleogeographic positions that underpin deep time climate, oceanographic, and biologic research. Paleomagnetic data are also widely used to reconstruct tectonic motions of deformed terranes found in accretionary orogens, such as the Tibetan Plateau, relative to stable plates such as Eurasia or India, to estimate pre-orogenic motion of plates, and the formation and destruction of ocean basins that have been lost to subduction (e.g., Zhu et al., 2013; Li et al., 2016; van Hinsbergen and Schouten, 2021). But when paleomagnetic data are used to develop such tectonic reconstructions, it is important to realize that there are two processes that together determine the absolute position relative to the geodynamo: plate tectonic motions relative to the mantle, and the combined rotation of lithosphere and mantle relative to the spin axis due to changes in Earth's moment of inertia, i.e., True Polar Wander (TPW) (Gold, 1955) (Fig. 1). To identify the signal of plate motions, the effects of TPW somehow need to be taken into account and corrected for (e.g., Steinberger and Torsvik, 2008).

Changes in the Earth's density structure that cause TPW may result from, for example, changes in subduction configuration or plume motion (e.g., Steinberger and Torsvik, 2010). The magnitude of TPW can be estimated from the difference between paleomagnetic reference frames that estimate motions of the global plate circuit relative to the Earth's spin axis and mantle reference frames that constrain plate motions relative to the mantle (e.g., Doubrovine et al., 2012), or from a common rotation of the entire plate circuit relative to an equatorial Euler pole (Steinberger and Torsvik, 2008; Torsvik et al., 2014). Such estimates suggest more than 20° of TPW in Triassic to Jurassic time on a ∼100 Myr timescale (Torsvik et al., 2008, 2012) (Fig. 1). In addition, some paleomagnetic and stratigraphic observations have been interpreted as even faster TPW events on a 10 Ma timescale in the late Jurassic (Muttoni et al., 2005; Kent and Irving, 2010; Mattei et al., 2014; Yi et al., 2019; Fu et al., 2020), although this is not beyond controversy (Kulakov et al., 2021). Although TPW may be estimated for plates tied together in a plate reconstruction based on marine geophysical data from the ocean floor, it is not possible to do this for individual tectonic terranes; that is, it is not possible to objectively discern between the effects of TPW and plate motion on the paleomagnetically determined positions of a terrane (e.g., Gao et al., 2021).

The northward drift of the Lhasa block of southern Tibet, from northern Gondwana to the southern margin of Eurasia, occurred during the Jurassic (Li et al., 2016) and overlapped with the late Triassic to early Jurassic TPW event of ∼20° (Torsvik et al., 2012). This drift history is constrained by geological and paleomagnetic evidence. The Lhasa terrane was located adjacent to northern Gondwana in late Triassic time, with rifting starting around 235 Ma (Zheng et al., 2022), and northward drift occurring mostly

after ~215 Ma (Zhu et al., 2011; Li et al., 2016). The Lhasa terrane collided with the Qiangtang terrane of southern Tibet in early Cretaceous time, around 130 Ma (Li et al., 2016; Li et al., 2019). During the first half of this northward drift history, the purported TPW would have moved the entire eastern Tethyan realm coherently southward at a rate of 5-8 cm/a (Fig. 1).

In this paper, we aim to develop an approach to overcome the difficulty of TPW in terrane reconstructions. In earlier work of our group (Li et al., 2016), we showed a high-quality paleomagnetic pole that placed the Lhasa terrane around an equatorial latitude at 180 Ma and estimated a paleolatitude path for Lhasa's northward flight assuming a constant motion rate relative to the spin axis. Combined with TPW, however, this would require that northward plate motion rates nearly doubled during and shortly after the TPW event. In this paper, we test whether this plate motion rate doubling is correct, or whether plate motion rates were near-constant, in which case TPW would produce an apparent paleolatitudinal stand-still of the Lhasa terrane in the Jurassic (Fig. 1).

Here we report a precisely dated volcanic-based paleomagnetic pole with from the Upper Jurassic of the Lhasa terrane that is ~25 Ma younger than the 180 Ma pole of Li et al. (2016). If we assume a constant paleolatitudinal drift rate, then we predict a paleolatitude of ~10-15°N at ~155 Ma. In contrast, if we assume a constant plate motion rate (with accounts for TPW), then a near-equatorial latitude would be expected. We use the paleomagnetic record of the Lhasa terrane to test which of these two end-member solutions is more likely. We evaluate the impact of TPW on paleomagnetic signals of past plate motion and discuss the potential of additional paleomagnetic data from the Lhasa terrane to further test the magnitude and viability of proposed latest Jurassic TPW.

2. Geological setting

The Lhasa terrane of southern Tibet is bounded by the Bangong-Nujiang suture zone (BNSZ) to the north, where the Mesotethys Ocean subducted in the Triassic to early Cretaceous, and the Indus-Yarlung Zangbo suture zone (IYZSZ) to the south, where the Neotethys Ocean subducted in Cretaceous to Paleogene time (Hu et al., 2016; Kapp and DeCelles, 2019) (Fig. 2). Prior to the arrival of continental lithosphere of the Indian plate at the south Tibetan trench, the Lhasa terrane was an Andean-type orogen associated with a widespread magmatic arc that was active during both the closure of Neotethys and Mesotethys (Zhu et al., 2011, 2013; Ding et al., 2013; Kapp and DeCelles, 2019).

The Lhasa terrane comprises a Neoproterozoic to Cambrian crystalline basement, a Paleozoic to Mesozoic marine stratigraphic cover, and Mesozoic and Cenozoic arc magmatic rocks and terrestrial sedimentary basins (Zhu et al., 2013). The Paleozoic and older sequence contains faunal and compositional characteristics that compare well with northern Gondwanaland (Torsvik and Cocks, 2009). Although there may well have been relative motion between the Lhasa block and northern Gondwana in late Paleozoic time, the final onset of its northward flight toward the Tibetan margin is estimated at late Triassic based on stratigraphic, geochemical, and paleomagnetic measurements (Zhu et al., 2011, 2013; Li et al., 2016; Zheng et al., 2022). Among these previous paleomagnetic datasets are three paleopoles from the Jurassic of the Lhasa terrane: the high-quality, 180 Ma lava-based paleomagnetic pole from Sangri (Li et al., 2016) and two poles reported in Chinese literature, based on 21 limestone samples (Zhu, 1985) and 32 limestone samples (Dong et al., 1991). These latter two studies were not evaluated for inclination shallowing and remagnetization, and no field tests were reported, so the quality of these poles is difficult to assess, but given the sparsity of data, we show them in our diagrams for illustration.

Our study area is near Xungba Town, Geji County within Ngari area, in western Tibet (Fig. 2). Here we sampled the Upper Jurassic Zenong volcanics. This unit comprises the base of a sequence of volcanic and marine and terrestrial sedimentary rocks whose deposition continued into the Cenozoic. At our study location, the sampled lavas are predominantly basalts and basaltic andesites (Figure S1 & Table S1). In previous studies and geological survey work, scholars assigned this suite of volcanic rocks (three geological sections presented in this study) to an age of ~30-20 Ma (i.e., Middle Oligocene-Early Miocene), which is equivalent to the Neogene Xungba Formation volcanics based on their distribution and typical rock types (e.g., Liu et al., 2011). Subsequent studies confirmed that some volcanic rocks from surrounding areas, but not the locations reported in our study, are indeed the Neogene Xungba Formation (~24 Ma in age) (e.g., Liu et al., 2011). For the purpose of unambiguously distinguishing the Upper Jurassic volcanic rocks from the Neogene Xungba Formation volcanics, we dated each sampling locality using U/Pb zircon radiochronology (see below) and refer to the suite of volcanic rocks as the Upper Jurassic-Lower Cretaceous Zenong Group volcanic rocks.

In the field, the Zenong Group lavas occur as ~200 m-thick stacks of flows that are each ~5-meters thick. Lavas have discrete or variably distinct flow tops and interbedded tuffaceous sediments. These units are folded and thrusted in the NW-SE trending Bangba fold and thrust belt, and they are unconformably overlain by the mostly undeformed, widespread Neogene Xungba Formation volcanic rocks. (Fig. 2; Figure S1 and Table S1 in Supporting Information).

3. Sampling and methods

We collected 419 paleomagnetic samples from 49 lava sites distributed over three sections of the Upper Jurassic-Lower Cretaceous Zenong Group volcanics (GPS, 32.0°N, 82.0°E) (Fig. 2; Figure S1 and Table S1 in Supporting Information). Thirteen sampling sites are from Section 1; twenty-five sites are from Section 2, which is ~10 km southwest of the Section 1; eleven sites are from Section 3, ~20 km southwest of Section 2 (Fig. 2; Figure S1 and Table S1). The lavas of the three sections are folded and variably strike NE to NW and dip 10-50°. We assume an original horizontal orientation of the lavas. Bedding attitudes for sampled Upper Jurassic volcanic outcrops were measured using a magnetic compass. Between 1 and 3 flow-top attitude measurements were made at each site and then averaged for each tilt correction.

We collected 6-10 independently oriented paleomagnetic samples at each sampling site using a portable gasoline-powered drill; samples were collected over ~1 m of outcrop. All paleomagnetic samples were oriented using a magnetic compass and when possible, a sun compass was used to assess any local magnetic anomalies. The differences between readings of the two compasses are limited to ±2°. Bulk samples of 1-3 kg each were collected from basalts and basaltic andesites at Sections 1, 2, and 3 for U/Pb zircon dating (2019GX08, 2019GX20, and 20GXC09) (Fig. 3; Figures S1, S2, and Table S2).

4. Zircon U-Pb dating

We analyzed 51 zircon grains from the three basalt/basaltic andesite samples. Measurements were completed at the Key Laboratory of Continental Collision and Plateau Uplift (now part of the State Key Laboratory of Tibetan Plateau Earth System and Resources Environment), Institute of Tibetan Plateau Research, Chinese Academy of Sciences. Crystal morphology is mostly euhedral and subhedral prismatic. Selected zircons were visually characterized with cathodoluminanescence to reveal internal structures. These zircons exhibit typical oscillatory zoning which is consistent

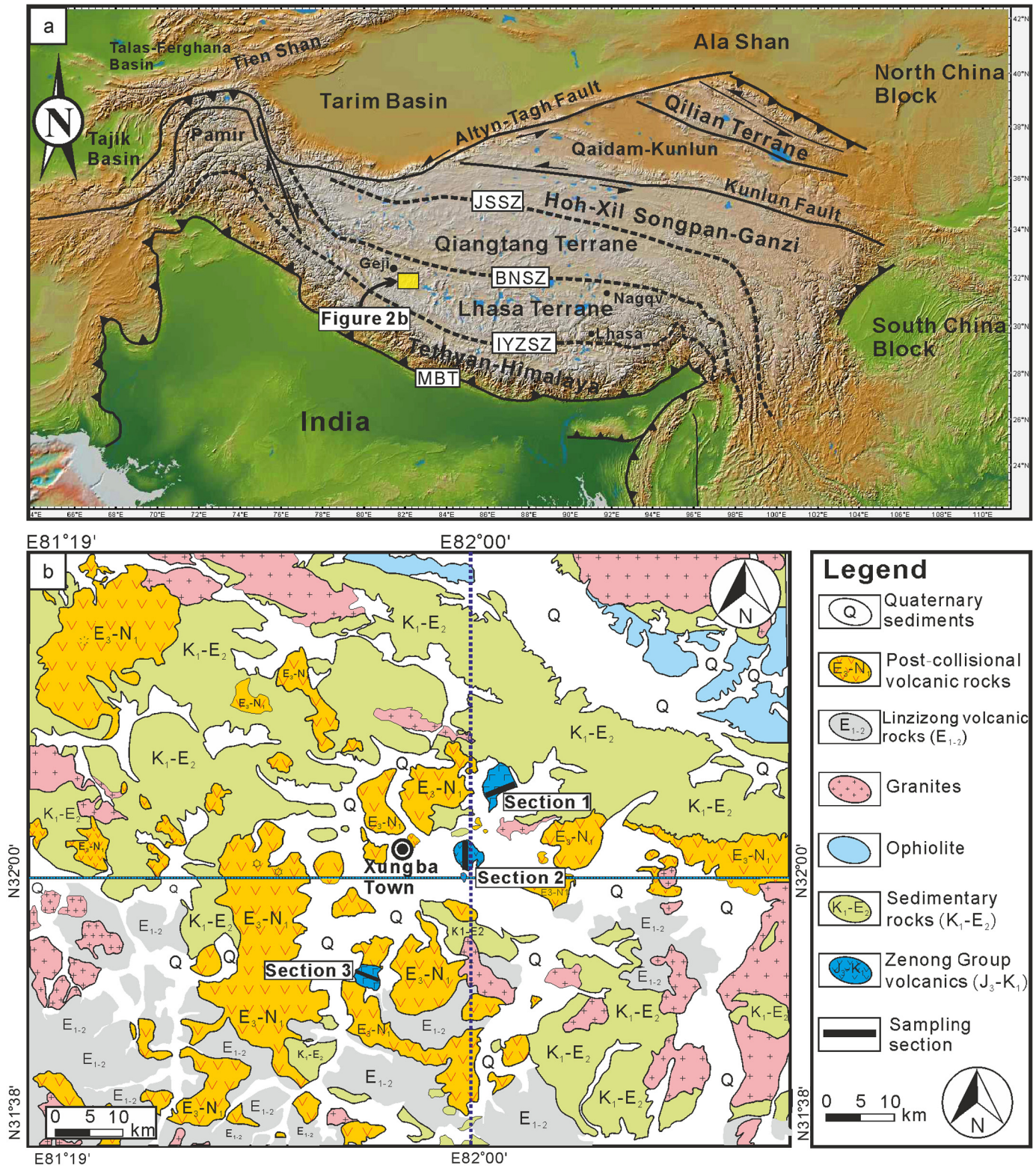

Fig. 2. (a) Shaded relief map of the Tibetan Plateau and surrounding region with tectonic blocks and major boundaries indicated. The Zenong Group volcanics in study area within the Geji County, Ngari area is located in western Lhasa terrane of central Tibet (enclosed by small yellow rectangle). Abbreviations are as follows from south to north, MBT: Main Boundary Thrust; IYZSZ: Indus-Yarlung Zangbo Suture Zone; BNSZ: Bangong-Nujiang Suture Zone; JSSZ: Jinsha Suture Zone. (b) Detailed Geological map of the study area near Xungba Village in Ngari County (scale, 1:250,000). Three black-filled rectangles indicate the locations of the three sampling sections in this study.

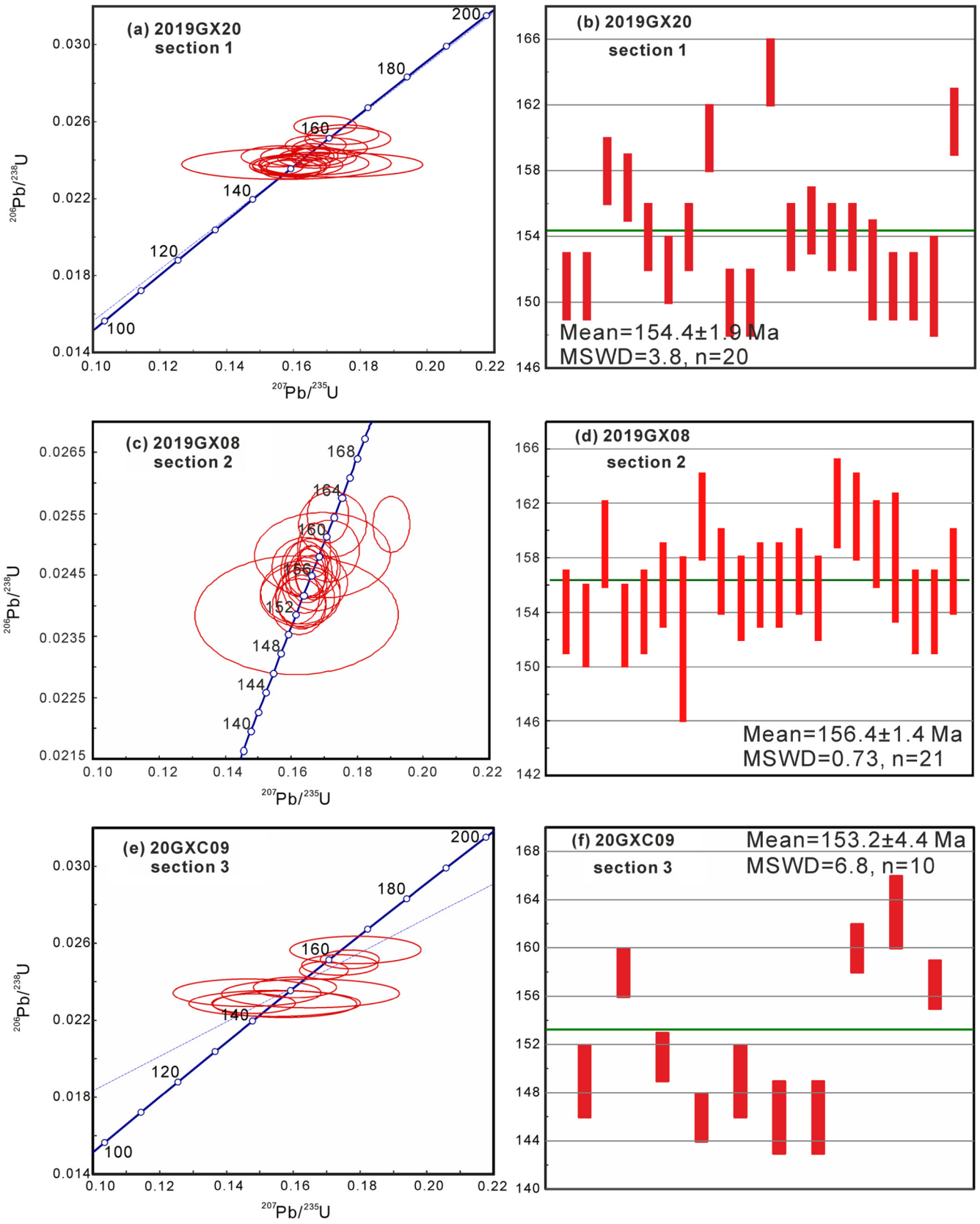

Fig. 3. Isotopic ratios and corresponding U-Pb ages from zircons extracted from three bulk samples of the Upper Jurassic-Lower Cretaceous Zenong Group volcanic rocks. Data were collected using laser-ablation inductively-coupled plasma mass spectrometry. Samples 2019GX20, 2019GX08, and 20GXC09 were collected from sections 1, 2, and 3, respectively. (a) Concordia plot of U-Pb results from 20 zircon grains of bulk sample 2019GX20 (Section 1); (b) Distribution of ages and weighted mean age for sample 2019GX20; (c) Concordia plot of U-Pb dating results from 21 zircon grains of bulk sample 2019GX08 (Section 2); (d) Distribution of ages and weighted mean age for sample 2019GX08; (e) Concordia plot of U-Pb dating results from 10 zircons of bulk sample 20GXC09 (Section 3); (f) Distribution of ages and weighted mean age for sample 20GXC09. See Table S2, Text S2, and Figure S2 in Supplementary Information for detailed data and procedures.

with a magmatic origin (Figure S2). Th/U ratios for three samples range from 0.14 to 1.52, with a mean Th/U ratio of 0.64 (Table S2).

Full details of the instrumentation, standards, software, and procedures used to collect and interpret U and Pb isotopic data are provided in the Supplemental Information (Text S2, Figure S2, and Table S2). Weighted mean ages for these three bulk samples are 154.4±1.9 Ma (MSWD=3.8, n=20), 156.4±1.4 Ma (MSWD=0.73, n=21), and 153.2±4.4 Ma (MSWD=6.8, n=10) (Fig. 3; Text S2 and Table S2). We interpret these ages to record crystallization ages for the Upper Jurassic-Lower Cretaceous Zenong Group volcanic rocks.

5. Petrography and magnetic mineralogy

We used non-destructive and semi-quantitative petrographic investigations to examine textures and mineral compositions, grain shapes and sizes, and mineral distributions in 9 samples (Table S3). These specimens were prepared as polished thin sections (Figures S3 and S4).

We conducted Raman spectroscopy at the Key Laboratory of Mineral Resources, Institute of Geology & Geophysics, Chinese Academy of Sciences to characterize the composition, grain size, and distribution of rock forming minerals. We also examined opaque minerals (e.g., magnetite and hematite) in thin section under reflected light (Text S3, Figures S3 and S4). Distinct peaks corresponding to wavenumbers of 670-690 cm^{-1} identify the presence of magnetite (Figure S3), whereas peaks corresponding to wavenumbers of 410-420, 290-310, and ~230 cm^{-1} correspond to hematite. Hematite is most abundant in specimens 20GXC04 and 20GXC07 (Figure S3). Magnetite and hematite were identified under reflected light as irregular bright spots. We did not observe any degraded mineral margins that would be consistent with low-grade metamorphism or penetrative weathering. Instead, unaltered magnetite particles coexist with feldspar, quartz, and pyroxene (Figures S3 & S4).

Temperature-dependence of magnetic susceptibility (χ-T) (Figure S5) was measured at the Key Laboratory of Paleomagnetism and Tectonic Reconstruction of Ministry of Natural Resources, Institute of Geomechanics, Chinese Academy of Geological Sciences, Beijing, China. Measurements were completed using an MFK-1 Kappabridge (AGICO Instruments Company) equipped with a CS-4 high-temperature furnace. Crushed, coarsely powdered specimens were treated with a complete heating-cooling cycle from room temperature to the maximum temperature of 700°C in an air atmosphere in a field of 200A/m at a frequency of 976 Hz. (Figure S5). Each of the 23 samples analyzed exhibit a substantial decrease in magnetic susceptibility near the Curie temperature of magnetite (~585°C) (Figure S5). This behavior suggests that magnetite is the dominant remanence carrier in the studied samples. Notably, all samples except for GX19-8, GX23-2, and GXC09-1 exhibit that heating curves are higher than the associated cooling curves: this suggests no or only very limited occurrence of mineralogical transformations or generation of strong magnetic minerals by heating (e.g., exsolution of titanomagnetite to magnetite, or dehydration of clays (Dunlop and Özdemir, 1997)). Some samples also show a minor decrease of magnetic susceptibility between 590-680°C (e.g., GXC10-2, GXC12-7); these temperatures are within the range of the Neél temperature of Ti-bearing hematite (usually lower than 680°C), consistent with presence of Ti-poor titanohematite. The presence of titanohematite in some samples is supported by hysteresis loops, IRM acquisition curves, petrographic investigations, and stepwise thermal demagnetization results presented below.

Hysteresis loops, isothermal remanent magnetization (IRM) acquisition curves, and backfield demagnetization curves (Figures S6 and S7) were obtained using a Princeton Measurements Corporation Vibrating Sample Magnetometer (MicroMag^{TM} Model 3900 VSM) at the Beijing Paleomagnetism and Geochronology Laboratory of the State Key Laboratory of Lithospheric Evolution, Institute of Geology and Geophysics, Chinese Academy of Sciences in Beijing. Chips collected from cuttings of paleomagnetic specimens were crushed into smaller fragments for these measurements. Hysteresis loops (Figure S6) and IRM acquisition curves (Figure S7) were measured at room temperature over a magnetic field range of ±1.5 T for the same 23 samples for which χ-T curves were measured. All but three samples show hysteresis loops that completely closed by ≤0.2-0.3 T with low to moderate coercivity values ranging from 10.39 to 19.93 mT (mean value of 13.72±2.09 mT (n=20)). The saturation magnetization (M_s) ranges from 0.1148 to 1.235 Am^2/kg, with saturated remanent magnetization (M_{rs}) values of 0.02652-0.2391 Am^2/kg (Table S4). The three remaining samples exhibit typical wasp-waited hysteresis loops (Figure S6), suggesting the presence of two or more magnetic minerals with contrasting coercivities (i.e., existence of both low- and high-coercivity magnetic minerals grains such as magnetite and titanohematite) (Tauxe et al., 1996). For samples with wasp-waisted loops, coercivity is typically less than 20 mT (Figure S6 and Table S4). The corresponding IRM acquisition curves show a rapid increase from 0 to 200 mT, with acquisition of ~90% of the saturated IRM within this range, suggesting the presence of low-coercivity magnetic mineral grains. The IRM intensity for some samples (e.g., GX31-5, GXC13-2, and GXC17-1) increases gradually above 200 mT and saturation still is not fully reached at 1.5 T; these results indicate the presence of high-coercivity magnetic minerals like titanohematite in these samples (Figure S7).

Backfield demagnetization curves were measured at room temperature following measurement of IRM acquisition curves. We used a maximum magnetic field of 1.5 T, after which samples were demagnetized by applying a reversed magnetic field with magnetic field intensity up to as high as 0.2 T until the demagnetization curves overlap with the X-axis (Figure S7). The backfield demagnetization curves show that remanence coercivity (H_{cr}) is generally lower than 40 mT with an average value of 27.1±5.1 mT (n=23) for all twenty-three samples (Table S4); sample GXC06-5 is an exception. The M_{rs}/M_s ratio vs. H_{cr}/H_c ratio on the Day-plot (Figure S8) show that magnetic properties of most samples fall into the pseudo-single-domain region and generally follow the single domain (SD) and multi-domain (MD) mixing curves, which suggests mixtures of SD and MD magnetite particles (Dunlop, 2002), or, perhaps more likely, a population of stable vortex domain states (Roberts et al., 2017).

In summary, our rock magnetic data suggest that the dominant remanence carrier in the Zenong Group volcanics is stable single domain or vortex state magnetite. For a small portion of samples, low-Ti magnetite and hematite coexist. We find no obvious petrographic or rock magnetic evidence for alteration or secondary growth. Both minerals are common accessory minerals in volcanic rocks.

6. Paleomagnetic procedures and results

6.1. Procedures

Stepwise thermal or alternating field (AF) demagnetization procedures and measurements were completed for the first batch of specimens (including those containing sites of GX19-GX23, GX29-GX35) at the Paleomagnetism and Environmental Magnetism Laboratory at China University of Geosciences (Beijing). The second batch of paleomagnetic specimens from sites of GXC01-GXC20 were thermally demagnetized and measured at the Key Laboratory of Paleomagnetism and Tectonic Reconstruction, Ministry of Natural Resources, Institute of Geomechanics, Chinese Academy of Geological Sciences in Beijing. A third batch of paleomagnetic

specimens were subjected to either progressive thermal or AF demagnetization at the Paleomagnetic Laboratory of the Key Laboratory of Orogenic Belt and Crust Evolution, Ministry of Education, School of Earth and Space Sciences, Peking University in Beijing. In all three labs, progressive thermal or AF demagnetizations of the natural remanent magnetization (NRM) of all specimens was performed inside a magnetically shielded room with a residual field of <300 nT. An ASC-48 thermal demagnetizer, a D-2000 AF demagnetizer, and a JR-6A dual-speed spinner magnetometer (AGICO Instruments Company) were used to complete stepwise thermal or AF demagnetization and remanent magnetization measurements.

We designed our demagnetization schemes based on key information revealed by rock magnetism (χ-T curves) and petrographic investigations. During the initial stage of step-wise demagnetization experiments, we used thermal cleaning to demagnetize all specimens from the three sections; this method worked well for those specimens from Sections 1 & 2 until the maximum unblocking temperature (e.g., 575-655°C) was approached. However, in the process of step-wise demagnetization for specimens of Section 3, we noticed that the intensity of the remanent magnetizations for most specimens decreased rapidly and the magnitudes were reduced to < 50% of the NRM at temperatures of 200°C. Therefore, we applied a hybrid demagnetization scheme to these samples, in which we thermally demagnetized specimens up to 240-250°C, and then used AF demagnetization up to 150 mT to clean the remaining remanent magnetization. In short, this hybrid step-wise demagnetization technique worked well for specimens from Section 3.

6.2. Paleomagnetic results and statistical analysis

Thermal and AF demagnetization (or hybrid demagnetization) results were projected onto orthogonal vector diagrams (Fig. 4) for further analysis using principal component analysis (Kirschvink, 1980) with the PaleoMac software. Additional statistical analysis for ChRM directions and low-temperature directional components (LTCs) (Fisher, 1953) (Fig. 5; Figure S9), a non-parametric fold test (Tauxe and Watson, 1994) (Fig. 5c), and a synfolding test (Figure S10) were conducted using the PmagPy software package (Tauxe et al., 2016, https://earthref.org/PmagPy), the online paleomagnetic analysis portal Paleomagnetism.org (version 2.2.0) (Koymans et al., 2016), and PMGSC software (version 4.2).

The intensities of high-temperature/high-field components (HTC/HFC) for 181 of 332 specimens straightforwardly decay to the origin after removal of a low-temperature component (LTC) below 300-350°C (Fig. 4; Figure S9). The *in situ* mean direction of the LTCs is $D_g/I_g = 356.5°/52.2°$, k_g=23.0, α_{95g}=2.2° (n=181), which is similar to the present geomagnetic field (PGF, D/I=1.55°/50.2°) and the present dipole field (PDF, D/I=0.0°/51.3°) directions at the sampling site (32.0°N, 82.0°E) (Figure S9). Moreover, the grouping of the LTCs disperse significantly after tilt correction (Figure S9). The consistency of the isolated LTCs and their mean direction with the PGF and the PDF directions suggests a post-folding remanence acquisition for the LTC. We interpret the LTC as a recent viscous overprint by the present geomagnetic field. (Figure S9).

A high temperature/high field (HT/HF) component that decays toward the origin is interpreted as the Characteristic Remanent Magnetization (ChRM) if it is resolved by at least 4 consecutive temperature/AF steps from 400/450°C up to 575/595°C and/or 625/655°C or from 10mT up to 80-120 mT or higher. Almost all specimens from Section 1 were thermally demagnetized up to 575-595°C, consistent with magnetite as the dominant remanence carrier. Specimens from Section 2 record directions that decay toward the origin up to 625-655°C, consistent with the presence of Ti-poor titanohematite as a remanence carrier. For the specimens from Section 3, ChRMs are typically interpreted from 10 mT to 80-150 mT or even 180 mT (Table 1; Fig. 4); these results are consistent with the presence of magnetite. Three of 49 sites yielded no interpretable results (GXC19, GXC29, and GXC30). The interpreted ChRM directions from the remaining 46 sites were combined without further filtering (following Gerritsen et al., 2022) and are listed in Table 1.

We applied the following procedure to calculate a locality mean direction and paleolatitude from our 46 site mean directions. First, we rotated all site-mean directions to a northwest declination, which we interpret as a counterclockwise rotated normal polarity direction. Each site-mean direction then was converted to a VGP. The Fisher mean paleomagnetic pole for the 46 VGPs is located at $\lambda_p = 45.3°$N, $\varphi_p = 295.3°$E, with K=69.8 and $A_{95} = 2.5°$ (Table 1). Finally, we calculated the corresponding paleomagnetic direction at the representative sampling location (32.0°N, 82.0°E) as $D \pm \Delta D_x = 337.1 \pm 2.6°$, $I \pm \Delta I_x = -13.8 \pm 4.9°$, and $\alpha_{95} = 4.9°$.

The VGP distribution is just below the limit of what is expected for paleosecular variation (PSV) of the magnetic field. The A_{95} of the mean pole is 2.54, compared to 2.59 that is expected for a population of 46 poles (Deenen et al., 2011); this suggests that PSV is slightly under sampled. The straightforward explanation for this is that some stratigraphically adjacent site-mean directions overlap with each other (Fig. 5a, b), suggesting that these consecutive lavas were erupted within a time-frame such that the some spot readings may be present in the data set twice. Some authors choose to bin data of consecutive lavas if their directions statistically overlap (e.g., Lippert et al., 2011). However, because such filters have minimal impact on the position and distribution statistics of the calculated pole (Gerritsen et al., 2022), we choose to use the mean of our 46 sites as the basis for our further analysis.

The 46 site-mean directions pass a bootstrapped fold test with optimal clustering at 86-107% unfolding (Tauxe and Watson, 1994) (Fig. 5c). A parametric simulation synfolding test also indicates that the precision parameter k reached its maximum value of 51.97 at 93.7±1.6% unfolding (Figure S10). The dataset passes the parametric reversal test of Tauxe (2010).

Therefore, we conclude that the Upper Jurassic Zenong volcanics acquired their magnetization prior to folding. Given the petrographic and mineral magnetic evidence suggesting primary mineralization of the remanence carriers, we conclude that the paleolatitude calculated from the paleomagnetic pole on the basis of 46 tilt-corrected site-mean directions represents the position of the Lhasa terrane relative to the Earth's spin axis at 155±2 Ma.

7. Discussion

7.1. Trench migration rates

Our paleomagnetic pole from the Zenong Group volcanics indicates that the Lhasa terrane was positioned at 7.0 (+2.5, −2.5)° S at 155±2 Ma. This near-equatorial, southern hemisphere latitude is similar to latitudes calculated from older Jurassic rocks on the Lhasa terrane, including the 180 Ma old Sangri Group lavas (Li et al., 2016). Taken together, these data suggest that the Lhasa terrane remained at a near-stationary, subequatorial position throughout much of the Jurassic despite its plate tectonic migration from the northern Gondwana margin to the southern margin of Tibet.

This result contradicts our earlier motion path of the Lhasa terrane (Li et al., 2016) that assumed a constant paleolatitudinal drift rate. It is, however, more consistent with the predicted path assuming constant spreading rates between Lhasa and northern Gondwana. If Lhasa moved from the northern Indian to the southern Eurasian margin between 215 and 130 Ma at a constant motion rate, then plate reconstructions of India *versus* Eurasia (e.g., Müller et al., 2018) show that a Neotethys spreading rate of ~8 cm/a is required. To evaluate the robustness of this result, we

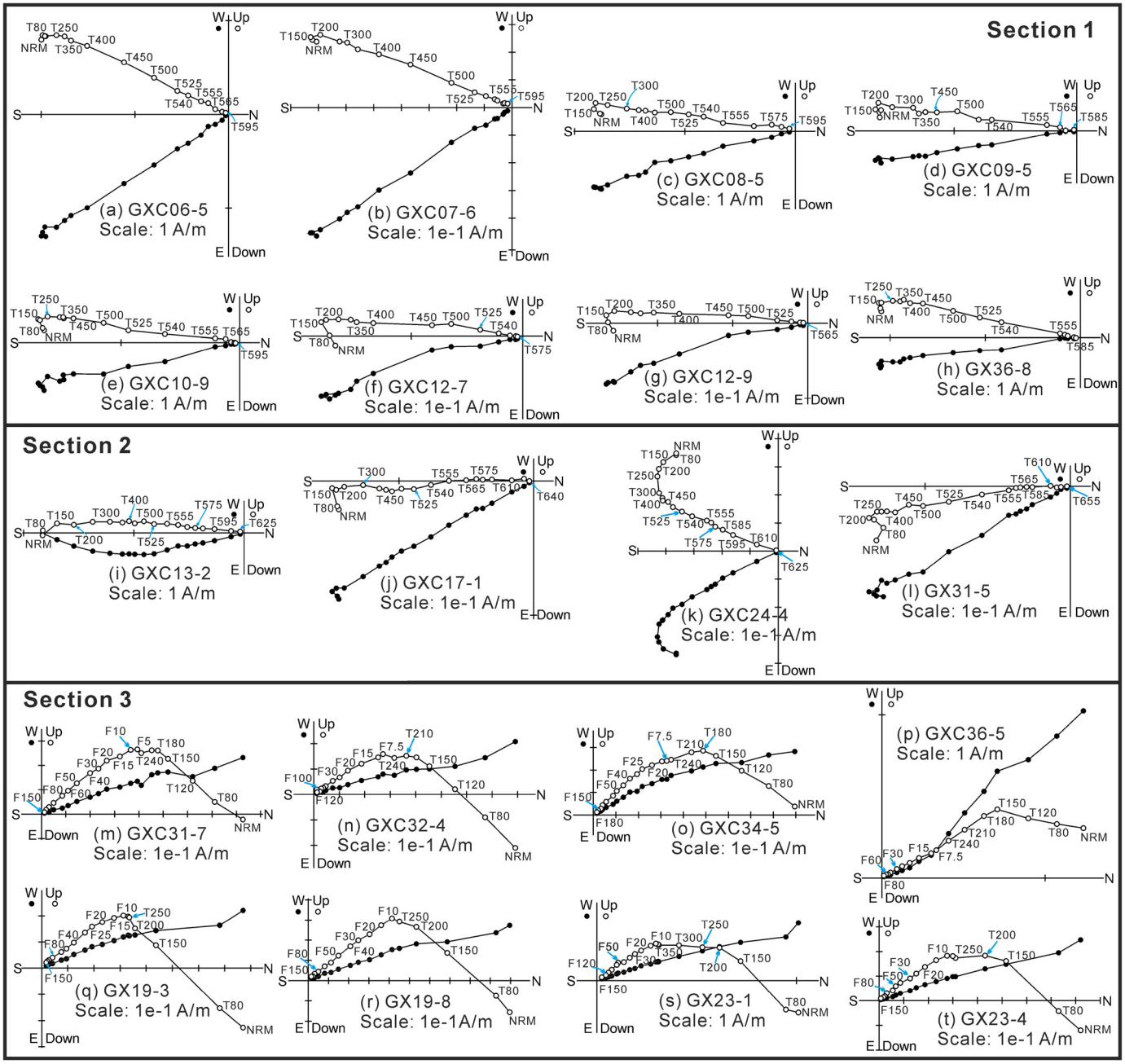

Fig. 4. Orthogonal vector projection of results from thermal/alternating field demagnetization for representative specimens; all plots are presented in geographic coordinates. Closed (open) circles represent projection of vector end-points onto horizontal (vertical) plane. For instance, T500 indicates a thermal demagnetization step of given magnitude in °C, whereas F50 indicates an alternating field demagnetization step of given magnitude in mT.

place our reconstruction of constant plate motion rate of Lhasa relative to India (between 215 and 130 Ma) in three formulations of the global APWP: that of Torsvik et al. (2012), Besse and Courtillot (2002), and Kent and Irving (2010). We built this reconstruction in the GPlates plate reconstruction software (Müller et al., 2018) and used Paleomagnetism.org (Koymans et al., 2016) to rotate the APWPs in the coordinates of the reconstructed Lhasa terrane following procedures described in Li et al. (2017) (Figs. 6 & 7). Here, for ease of comparison, we show curves of paleolatitudes that vary as a function of geological time, which were calculated from our selected APWPs (Besse and Courtillot, 2002; Kent and Irving, 2010; Torsvik et al., 2012) in Indian and Eurasian coordinates, for our reference location (29.5°N, 92°E) (Fig. 7). Each of the three APWPs predict the 180 and 155 Ma paleolatitudes of the Lhasa terrane calculated from the Zenong and Sangri poles. We conclude that the presently available paleomagnetic data of the Lhasa terrane are successfully explained by a constant ~8 cm/a northward motion rate of the Lhasa terrane relative to India.

This constant drift rate of the Lhasa terrane relative to the mantle provides an important constraint on the long-lived trench migration rate associated with subduction below the Lhasa terrane. Arc magmatism on the Lhasa terrane in the Late Triassic to Early Cretaceous is interpreted to reflect subduction below the Lhasa terrane during its northward motion toward Eurasia. Whether this occurred through roll-back (if subduction was southward below the northern Lhasa terrane, the scenario we favor), or slab advance (if subduction was northward below the southern Lhasa terrane) remains unresolved by our data. Regardless of the mechanism, the

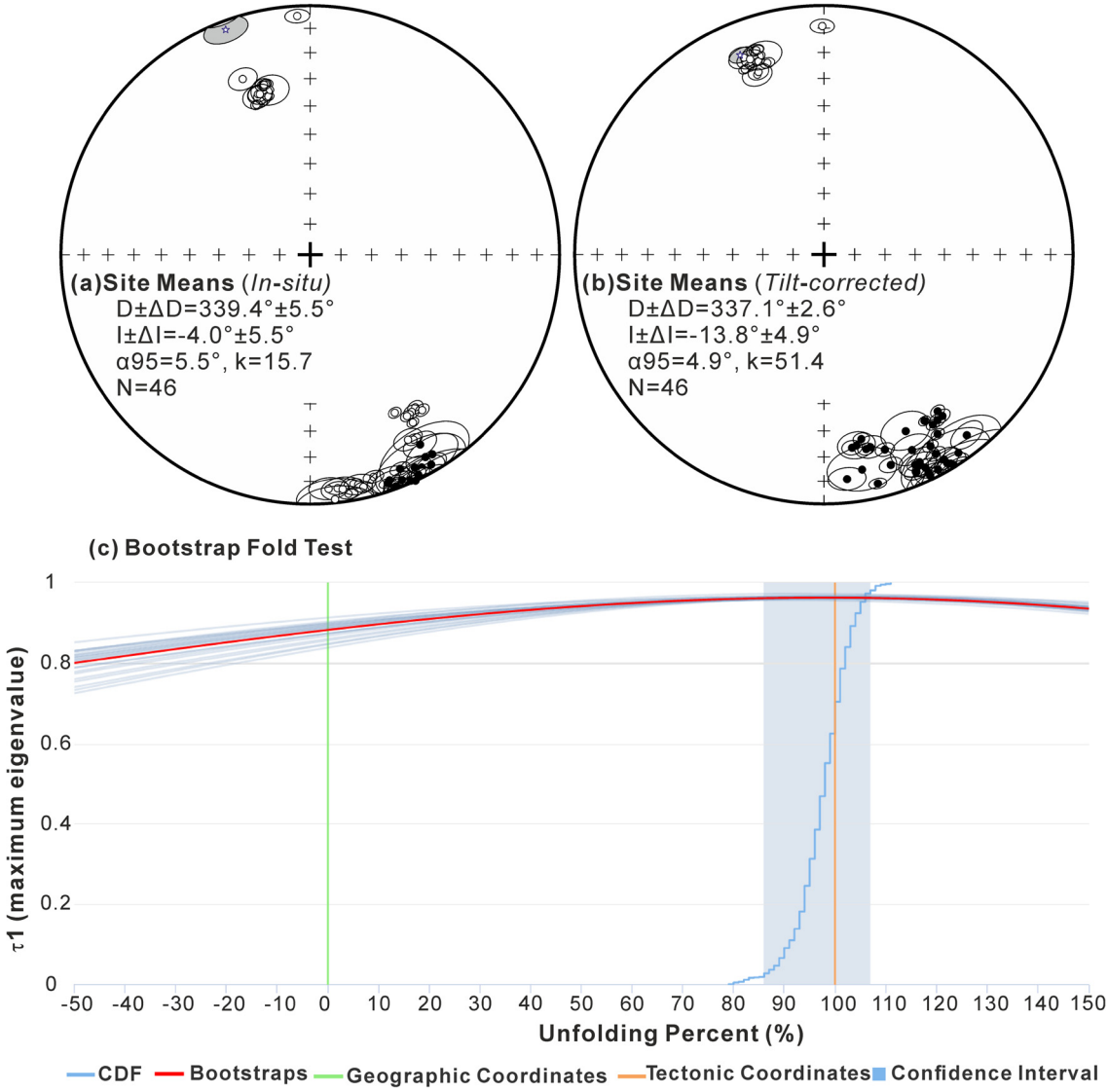

Fig. 5. Equal-area projections of paleomagnetic directions of the Upper Jurassic volcanic rocks with Fisher means and corresponding 95% confidence ellipses before (a) and after (b) tilt correction and (c) corresponding bootstrap fold test results. (a,b) Equal-area projections of 46 site-mean directions (see text for details) before and after bedding corrections. Solid and open symbols represent projections onto lower and upper hemisphere, respectively. Open stars with light grey-colored ellipses show the mean directions and the 95% confidence limits before and after bedding correction. (c) Results from a non-parametric bootstrap fold test using 1000 resamplings of the data (Tauxe and Watson, 1994). The highest eigenvalues $\tau 1$ are calculated between 86 and 107% unfolding level (vertical grey bar in figure), consistent with a pre-folding magnetization.

trench and slab must have moved at ~8 cm/a. For comparison, the South American plate has advanced westward above a retreating Nazca slab at 2 cm/a over the last 50 Ma (Oncken et al., 2006; Schepers et al., 2017). On the other hand, van de Lagemaat et al. (2018) showed that the northward motion of the Tonga slab is undergoing slab-parallel dragging at ~4 cm/a and the Burma slab is presently moving at similarly high velocities (van de Lagemaat et al., 2018; Parsons et al., 2021). Less well-constrained, but similarly high roll-back rates have been reconstructed for the Olyutorsky Arc from the Late Cretaceous to Eocene (Vaes et al., 2019). Given that the rate of trench migration reconstructed here for the Lhasa terrane is four times higher than the rates reconstructed for the Andes, we predict that there are unexpected and hitherto unrecognized relationships between crustal deformation, trench migration, and magmatism that merit more attention (Oncken et al., 2006; Schepers et al., 2017). Moreover, we suggest that such long-lived trench migration rates may provide an interesting new constraint on the dynamics governing microcontinent formation and migration.

7.2. Late Jurassic true polar wander and plate motion

The stable paleolatitude of the Lhasa terrane during the Jurassic underscores the influence of true polar wander on paleogeography. Gao et al. (2021) recently used paleomagnetic data from the North China Block to show that changes in paleolatitude should not immediately be interpreted as a plate tectonic signal. The global APWP of Torsvik et al. (2012) is the only APWP presented here that quantified a TPW contribution (Fig. 7). In the Torsvik et al. (2012) APWP, the TPW contribution at 155 Ma is minimal; however, the equatorial latitude for the Lhasa terrane at 180 Ma is much higher than expected from plate tectonics alone. The clockwise rotation of the Earth relative to a pole that is presumed to be located at the equator around 11°E (Torsvik et al., 2014) cancels out much of the northward migration of the Lhasa terrane between 180 and

Table 1
Summary of sampling information and statistical site-means for resolved ChRM directions from the Upper Jurassic-Lower Cretaceous Zenong Group volcanic rocks in and around the Xungba Town, Geji County in Ngari area, far western Tibet.

Site ID	Strike/Dip	n/n$_0$	Direction						Paleopole position			
	(°)		Dg (°)	Ig (°)	Ds (°) (°)	Is	k (°)	α_{95} (°)	λp (°)	Φp	K (°)	A_{95}
Section 1												
GXC01	202/50	8/8	151.8	−28.9	147.6	15.9	882.7	1.9	39.4	305.3	/	/
GXC02	202/50	8/8	145.4	−26.6	143.7	20.8	599.0	2.3	34.9	307.2	/	/
GXC03	202/50	8/8	147.1	−25.9	145.5	20.6	526.7	2.4	36.1	305.5	/	/
GXC04	202/50	8/8	144.2	−24.2	144.0	23.4	718.0	2.1	34.0	305.8	/	/
GXC05	202/50	8/8	149.0	−25.5	147.3	20.1	870.2	1.9	37.3	303.9	/	/
GXC06	202/50	8/8	148.5	−22.2	148.8	23.1	1122.4	1.7	36.8	301.2	/	/
GXC07	253/30	8/8	150.8	−16.2	150.9	13.1	680.8	2.1	42.4	302.9	/	/
GXC08	282/31	8/8	164.1	−8.2	162.6	19.2	470.3	2.6	44.9	286.6	/	/
GXC09	282/31	7/7	169.3	−7.2	167.7	21.3	684.1	2.3	45.4	279.3	/	/
GXC10	282/31	8/8	173.3	−6.4	171.7	22.8	399.1	2.8	45.4	273.6	/	/
GXC11	282/31	8/8	170.9	−3.3	168.5	25.5	563.5	2.3	43.3	277.5	/	/
GXC12	282/31	8/8	168.2	−6.5	166.4	21.7	164.3	4.3	44.8	281.0	/	/
GX36	282/31	7/7	172.1	−5.7	170.3	23.4	134.8	5.2	44.8	275.4	/	/
Section 2												
GXC13	332/42	8/8	175.5	−6.5	174.1	10.4	133.9	4.8	52.3	271.6	/	/
GXC14	332/42	8/8	167.1	−5.0	166.7	6.3	650.0	2.2	52.6	284.2	/	/
GXC15	332/42	8/8	161.3	3.7	156.5	9.0	673.8	2.1	47.2	297.8	/	/
GXC16	332/42	8/8	160.4	3.7	155.7	8.3	137.7	4.7	47.1	299.1	/	/
GXC17	332/42	7/8	153.8	5.6	149.6	5.4	207.4	4.2	44.9	307.5	/	/
GXC18	332/42	5/8	150.0	3.3	148.3	1.1	369.4	4.0	45.8	310.9	/	/
GXC20	332/42	8/8	149.9	13.1	141.6	8.4	147.1	4.6	38.6	314.4	/	/
GXC21	332/42	8/8	156.0	0.9	154.4	3.3	827.0	1.9	48.5	302.7	/	/
GXC22	332/42	3/8	150.3	7.4	145.8	4.4	106.7	12.0	42.8	312.0	/	/
GXC23	332/42	2/8	152.3	4.2	149.4	3.3	454.4	11.7	45.6	308.7	/	/
GXC24	187/32	7/8	152.1	−17.2	148.7	2.2	232.3	4.0	45.6	309.9	/	/
GXC25	187/32	8/8	148.5	6.9	155.1	23.0	63.6	7.0	40.0	294.5	/	/
GXC26	187/32	7/8	152.6	−2.6	155.7	15.1	110.6	5.8	44.0	296.6	/	/
GXC27	187/32	8/8	356.9	−4.5	359.6	−9.1	341.7	3	53.4	262.7	/	/
GXC28	187/32	8/8	159.6	−1.9	162.3	12.5	339.0	3.0	48.1	288.9	/	/
GX29	332/42	5/5	174.2	−1.6	169.9	13.5	74.0	9.0	50.0	277.7	/	/
GX30	332/42	6/6	160.6	4.7	155.2	9.2	148.0	5.5	46.4	299.3	/	/
GX31	332/42	8/8	157.2	7.7	150.7	9.2	454.6	2.6	44.0	304.7	/	/
GX32	332/42	6/6	159.6	1.1	156.9	5.9	458.6	3.1	48.7	298.4	/	/
GX33	332/42	4/4	157.8	2.8	154.5	6.0	741.2	3.4	47.4	301.5	/	/
GX34	332/42	3/7	155.0	0.0	154.3	1.9	681.3	4.7	49.1	303.4	/	/
GX35	332/42	7/8	153.8	2.0	152.0	2.7	434.0	2.9	47.4	305.9	/	/
Section 3												
GXC31	47/17	8/8	342.3	−35.6	338.7	−20.0	850.1	1.9	43.1	291.2	/	/
GXC32	47/17	8/8	344.5	−29.9	341.4	−14.6	578.8	2.3	46.9	289.4	/	/
GXC33	52/10	8/8	345.4	−30.1	343.6	−20.9	735.6	2.0	44.5	284.7	/	/
GXC34	52/10	8/8	341.4	−33.6	339.7	−24.0	174.1	4.2	41.5	288.7	/	/
GXC35	52/10	8/8	342.0	−32.7	340.3	−23.2	366.7	2.9	42.1	288.3	/	/
GXC36	52/10	6/6	339.0	−25.4	337.9	−15.8	268.9	4.1	44.8	293.5	/	/
GX19	47/17	9/9	340.3	−36.2	336.9	−20.3	886.3	1.7	42.2	293.3	/	/
GX20	47/17	8/8	345.2	−34.6	341.3	−19.3	1181.8	1.6	44.5	288.2	/	/
GX21	47/17	8/8	346.3	−32.4	342.6	−17.3	103.0	5.5	46.0	287.0	/	/
GX22	47/17	9/9	344.8	−30	341.7	−14.7	702.5	1.9	46.9	289.0	/	/
GX23	47/17	9/9	342.6	−32.9	339.3	−17.3	208.1	3.6	44.7	291.3	/	/
Mean		**46/46 (325/332)**	**339.4**	**-4.0**	**337.1**	**-13.8**	**15.7 51.4**	**5.5 4.9**	**45.3**	**295.3**	**69.8**	**2.5**

Notes, **Strike/Dip,** right-hand strike direction of the bedding/dipping angle measured in the field; **n/n$_0$**, number of samples used to calculate site-mean direction/number of demagnetized samples; **Dg, Ig (Ds, Is)**, declination and inclination of statistical site-mean direction in geographic (stratigraphic) coordinates; **k**, best estimate of the precision parameter around the site-mean direction; **α_{95}**, radius of the site-mean direction at the 95% confidence level; **λp**, **Φp**, position of the calculated paleopole was based on observed ChRM site-mean direction at the sampling site (32.0°N, 82.0°E); **K,** precision parameter in calculating a paleopole; **A_{95}**, 95% confidence limit around a paleopole.

155 Ma. This creates a paleolatitudinal standstill over this time interval despite the ∼8 cm/a north-directed plate tectonic motion of the Lhasa terrane.

TPW reconstructed by Steinberger and Torsvik (2008)'s method occurs on timescales of 10's of Ma, because it uses the global APWP that is made with a 20 Ma sliding window at 10 Ma intervals. Muttoni et al. (2005) noted that such APWPs – including for example, Besse and Courtillot (2002) and Torsvik et al. (2012) – dampen or entirely mute the effects of TPW events that would occur on timescales shorter than 10 Ma. To highlight this, Muttoni et al. (2005) used a subset of paleomagnetic poles and abrupt and latitudinally-dependent changes in marine facies in sections in the Apennines (Italy) to argue for the occurrence of a substantial TPW event between ∼155 and 145 Ma. Muttoni and Kent (2019) tested this idea by using a shorter time interval and selecting only data for which inclination shallowing – a directional bias that is widespread in sedimentary rocks (Vaes et al., 2021) is corrected or can be excluded. The Kent and Irving (2010) APWP shows a sharp kink during the Jurassic (Fig. 7). Our 155 Ma pole is also consistent with Lhasa terrane APWP predicted from the Kent and Irving (2010) data (Fig. 7), in which there is a sharp kink in Jurassic time. We illustrate in Fig. 7 the potential for the Lhasa terrane

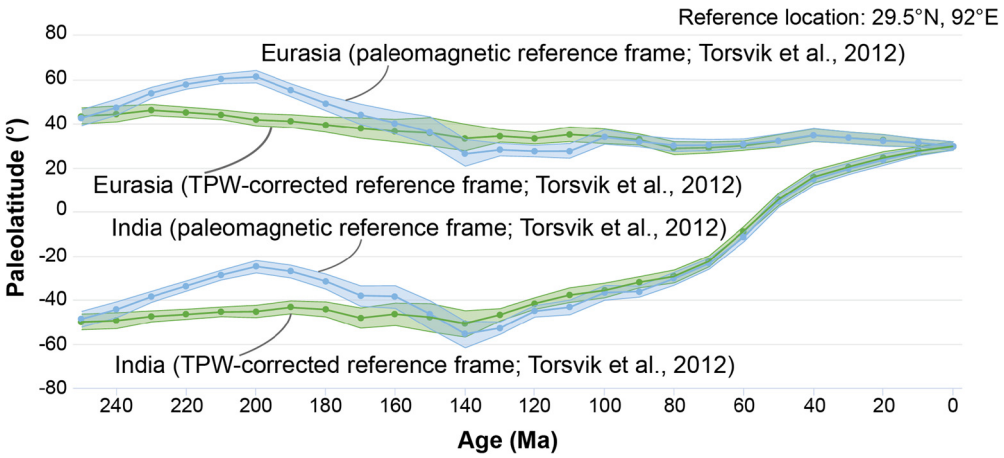

Fig. 6. Paleolatitude *versus* time for Eurasia and India for a reference position in southern Tibet near Lhasa City (29.5°N, 92°E). Paleolatitudes shown in green are calculated using the global apparent polar wander path (APWP) of Torsvik et al. (2012) with a true polar wander (TPW) correction, whereas those in blue are calculated using the same APWP without a TWP correction. The green curves predict latitudinal motion relative to the mantle, and the blue curves predict latitudinal motion relative to the Earth's spin axis and are the sum of plate motion *and* true polar wander. The Triassic-Jurassic, and late Jurassic-early Cretaceous intervals in which the green and blue curves diverge are intervals of TPW as inferred by Torsvik et al. (2012).

– with its Jurassic magmatic record – to provide another test of the late Jurassic TPW hypothesis. Importantly, if the conclusions of Kent and Irving (2010) are correct, then we expect that the Lhasa terrane moved southward by >15° during the Jurassic, despite its northward relative plate motion over this period (Fig. 1).

8. Conclusion

We have reported a new lava-based paleomagnetic pole for the Lhasa terrane from volcanic rocks dated to 155±2 Ma. Rock magnetic and petrographic analyses reveal that magmatic magnetite and Ti-poor titanohematite carry the magnetization. Moreover, there are no obvious signs of secondary magnetic mineralization in these rocks. Field tests indicate a pre-folding magnetization. We argue that the Zenong volcanics carry a primary magnetization that can be used in paleogeographic reconstructions. We calculate a paleomagnetic pole positioned at λ_p=45.3°N, φ_p=295.3°E with K=69.8 and A_{95}=2.5° based on 46 lava sites. The corresponding dipole direction at a reference location of 29.5°N and 92°E is D±ΔD=337.1°±2.6° and I±ΔI=-13.8°±4.9°, resulting in a latitude for the Lhasa terrane of 7.0 (+2.5, −2.5)° S at 155±2 Ma.

When combined with published paleomagnetic data for the Lhasa terrane, our results reveal a paleolatitudinal stand-still of the Lhasa terrane between 180 and 155 Ma. This result is consistent with predictions of several widely used global apparent polar wander paths *if* we assume a constant relative plate divergence rate between the Lhasa terrane and Gondwana (India) during its northward motion from Gondwana to Tibet in the late Triassic to early Cretaceous *and* an episode of >15° of true polar wander over the same time interval.

Previous workers have inferred that the Lhasa terrane was located above a subduction zone in the Late Triassic to Early Cretaceous. This subduction zone either dipped northward (which requires that the slab pushed northward through the mantle) or southward (which requires sustained slab rollback). Our results suggest that the rates of slab advance or retreat were ~8 cm/a, which is much higher than previously documented for convergent margins. For example, long-lived slab retreat in the Andes does not keep up with the 2 cm/a of upper plate advance, an imbalance that leads to Andean shortening. Although unprecedented in modern convergent margins, this example from the Lhasa terrane may provide a novel constraint on the rates at which slab migration through the mantle can occur. This proposition invites detailed studies of Jurassic magmatism and deformation of the Lhasa terrane's geology.

Finally, we conclude that the paleolatitudinal stand-still of the Lhasa terrane is the result of the interplay between Jurassic true polar wander, which translated the Lhasa terrane to more southerly latitudes, and its simultaneous northward plate tectonic motion which effectively masked much of the TPW in terms of absolute latitude. Our results can neither confirm nor reject the recently debated short-lived latest Jurassic-earliest Cretaceous TPW event known as the 'monster polar shift'. We note, however, that the Jurassic magmatic record, combined with our results confirming a simple plate kinematic scenario, highlights the significance of the Lhasa terrane as an ideal natural laboratory for evaluating the possible effects of short-lived TPW that may previously have been overlooked due to the long sliding window used for global APWP construction.

CRediT authorship contribution statement

L.D., Z.L., D.J.J.vH., and P.C.L. conceived key scientific ideas of the project and designed the geological mapping and sampling campaign in the field in central Lhasa area as well as made paleogeographic interpretation. Z.L. and L.D. were involved in the field work organization and sampling. Z.L., and T.Z. performed paleomagnetic measurements. Y.Y., Y.C., X.G., J.X., D.Z., and S.H. performed zircon U-Pb dating work, dating results analysis and optical observations for petrographic investigations. B.W. helped performed measurements of temperature-dependence of low-field susceptibility in the air atmosphere for representative rock samples; Z.L., D.J.J.vH., P.C.L., L.D., and H.L., performed paleomagnetic data analysis and the paleogeographic and tectonic interpretation and wrote the manuscript. All authors actively contributed to the interpretation of the results and the discussion of reconstructing paleolatitude of the Lhasa terrane in the Late Jurassic time.

Declaration of competing interest

The authors declare that they have no known competing financial interests or personal relationships that could have appeared to influence the work reported in this paper.

Acknowledgements

This study was jointly supported by the National Natural Science Foundation of China (NSFC) (grant no. 41972241, 41472185,

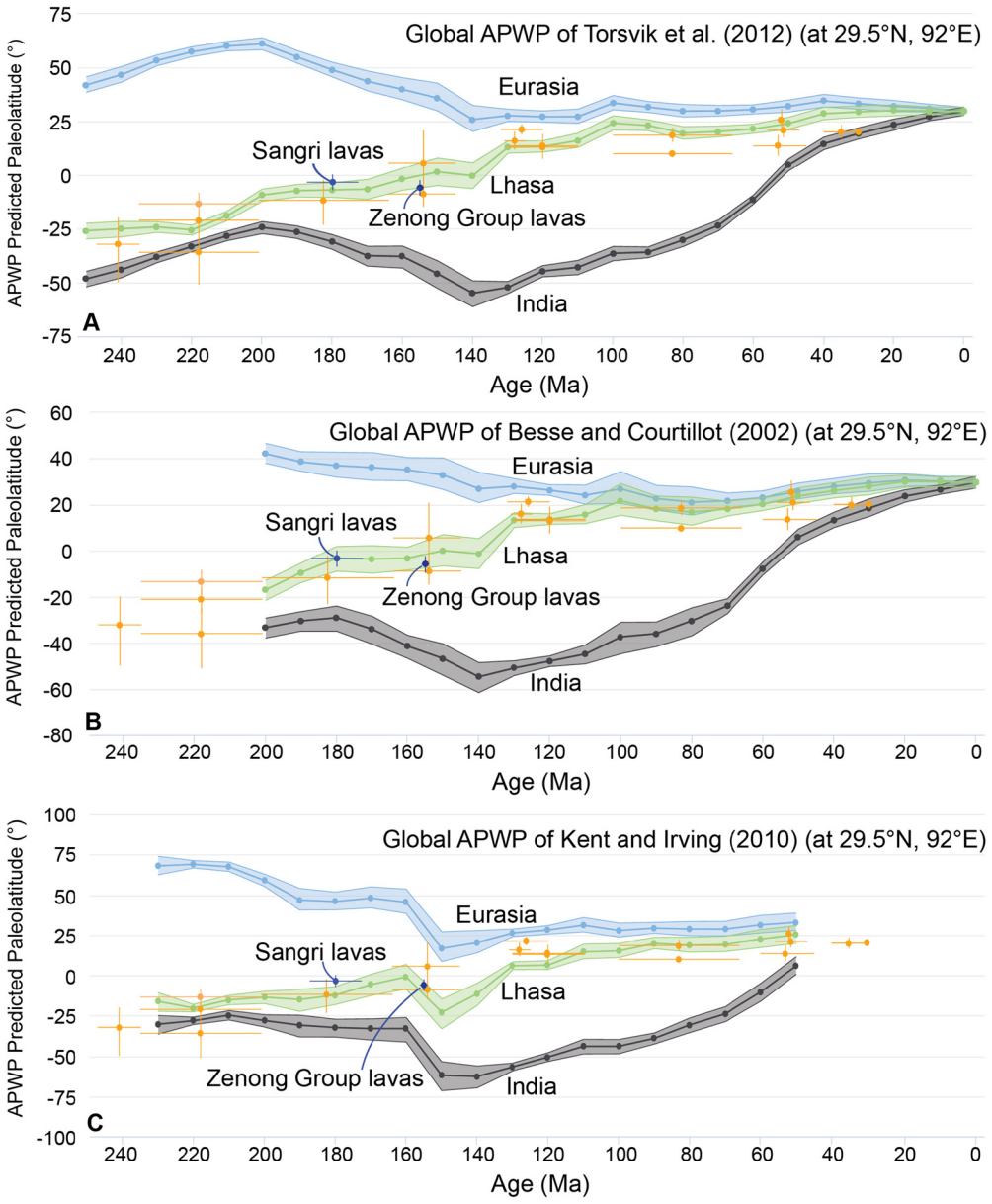

Fig. 7. Plot of paleolatitudes as a function of geological time for the Lhasa terrane (green APWP, individual orange data points), Eurasia (blue), and India (grey). Plots were made using http://www.paleomagnetism.org (Koymans et al., 2016). All data are provided in Tables S5 & S6 in Supporting Information. Eurasian and Gondwanan/Indian paleolatitudes are calculated from the reference poles of (A) Torsvik et al. (2012); (B) Besse and Courtillot (2002); and (C) Kent and Irving (2010).

41941016, and 41661134049), the Second Tibetan Plateau Scientific Expedition and Research Program (STEP) (Ministry of Science and Technology of China, 2019QZKK0708), and the Strategic Priority Research Program held by Chinese Academy of Sciences (Grant No. XDA20070301). D.J.J.vH. acknowledges NWO Vici grant 865.17.001. We thank handling editor Alex Webb and two anonymous reviewers whose comments helped clarify this manuscript. We benefited from constructive discussions with and technical assistance from Professors Bao-Chun Huang, Zhi-Ming Sun, Zhi-Dan Zhao, Hai-Yan Li, Yue Zhao, and Drs. Xiao-Zhou Ye, Qian Zhao, Neng-Tao Li, Xiao-Guang Li, Shuang-Chi Liu, and Cheng-Ying Liu. We are grateful to our driver for guidance with logistical support in the field.

Appendix A. Supplementary material

Supplementary material related to this article can be found online at https://doi.org/10.1016/j.epsl.2022.117609.

References

Besse, J., Courtillot, V., 2002. Apparent and true polar wander and the geometry of the geomagnetic field over the last 200 Myr. J. Geophys. Res. 107, EPM6-1–EPM6-31. https://doi.org/10.1029/2000JB000050.

Deenen, M.H.L., Langereis, C.G., van Hinsbergen, D.J.J., Biggin, A.J., 2011. Geomagnetic secular variation and the statistics of palaeomagnetic directions. Geophys. J. Int. 186, 509–520. https://doi.org/10.1111/j.1365-246X.2011.05050.x.

Ding, L., Yang, D., Cai, F.-L., Pullen, A., Kapp, P., Gehrels, G.E., Zhang, L.-Y., Zhang, Q.-H., Lai, Q.-Z., Yue, Y.-H., Shi, R.-D., 2013. Provenance analysis of the Mesozoic Hoh-Xil-Songpan-Ganzi turbidites in northern Tibet: implications for the tectonic evolution of the eastern Paleo-Tethys Ocean. Tectonics 32, 34–48. https://doi.org/10.1002/tect.20013.

Dong, X., Wang, Z., Tan, C., Yang, H., Cheng, L., Zhou, Y., 1991. New results of paleomagnetic studies of the Qinghai-Tibetan plateau. Geol. Rev. 37, 160–164.

Doubrovine, P.V., Steinberger, B., Torsvik, T.H., 2012. Absolute plate motions in a reference frame defined by moving hot spots in the Pacific, Atlantic, and Indian oceans. J. Geophys. Res., Solid Earth 117 (B09101), 1–30. https://doi.org/10.1029/2011JB009072.

Dunlop, D.J., 2002. Theory and application of the Day plot (Mrs/Ms versus Hcr/Hc) 1. Theoretical curves and tests using titanomagnetite data. J. Geophys. Res., Solid Earth 107 (B3). https://doi.org/10.1029/2001JB000486.

Dunlop, D.J., Özdemir, Ö., 1997. Rock Magnetism: Fundamentals and Frontiers. Cambridge University Press, Cambridge, pp. 74–76.
Fisher, R.A., 1953. Dispersion on a sphere. Proc. R. Soc. Lond. Ser. A 217, 295–305.
Fu, R.-R., Kent, D.V., Hemming, S.R., Gutiérrez, P., Creveling, J.R., 2020. Testing the occurrence of Late Jurassic true polar wander using the La Negra volcanics of northern Chile. Earth Planet. Sci. Lett. 529, 115835. https://doi.org/10.1016/j.epsl.2019.115835.
Gao, Y., Zhang, S., Zhao, H., Ren, Q., Yang, T., Wu, H., Li, H., 2021. North China block underwent simultaneous true polar wander and tectonic convergence in late Jurassic: new paleomagnetic constraints. Earth Planet. Sci. Lett. 567 (117012), 1–12. https://doi.org/10.1016/j.epsl.2021.117012.
Gerritsen, D., Vaes, B., van Hinsbergen, D.J.J., 2022. Influence of data filters on the position and precision of paleomagnetic poles: what is the optimal sampling strategy? Geochem. Geophys. Geosyst. 23, e2021GC010269.
Gold, T., 1955. Instability of the Earth's axis of rotation. Nature 175 (4456), 526–529.
Hu, X.-M., Garzanti, E., Wang, J.-G., Huang, W.-T., An, W., Webb, A., 2016. The timing of India-Asia collision onset - facts, theories, controversies. Earth-Sci. Rev. 160, 264–299.
Kapp, P., DeCelles, P.G., 2019. Mesozoic–Cenozoic geological evolution of the Himalayan-Tibetan orogen and working tectonic hypotheses. Am. J. Sci. 319 (3), 159–254. https://doi.org/10.2475/03.2019.01.
Kent, D.V., Irving, E., 2010. Influence of inclination error in sedimentary rocks on the Triassic and Jurassic apparent pole wander path for North America and implications for Cordilleran tectonics. J. Geophys. Res., Solid Earth 115 (B10103), 1–25. https://doi.org/10.1029/2009JB007205.
Kirschvink, J.L., 1980. The least-square line and plane and the analysis of paleomagnetic data. Geophys. J. Int. 62 (3), 699–718. https://doi.org/10.1111/j.1365-246X.1980.tb02601.x.
Koymans, M.R., Langereis, C.G., Pastor-Galán, D., van Hinsbergen, D.J.J., 2016. Paleomagnetism.org: an online multi-platform open source environment for paleomagnetic data analysis. Comput. Geosci. 93, 127–137.
Kulakov, E.V., Torsvik, T.H., Doubrovine, P.V., Slagstad, T., Ganerød, M., Silkoset, P., Werner, S.C., 2021. Jurassic fast polar shift rejected by a new high-quality paleomagnetic pole from southwest Greenland. Gondwana Res. 97, 240–262. https://doi.org/10.1016/j.gr.2021.05.021.
Li, S., Advokaat, E.L., van Hinsbergen, D.J.J., Koymans, M., Deng, C., Zhu, R., 2017. Paleomagnetic constraints on the Mesozoic-Cenozoic paleolatitudinal and rotational history of Indochina and South China: review and updated kinematic reconstruction. Earth-Sci. Rev. 171, 58–77.
Li, S., Yin, C., Guilmette, C., Ding, L., Zhang, J., 2019. Birth and demise of the Bangong-Nujiang Tethyan Ocean: a review from the Gerze area of central Tibet. Earth-Sci. Rev. 198 (102907), 1–25. https://doi.org/10.1016/j.earscirev.2019.102907.
Li, Z.-Y., Ding, L., Lippert, P.C., Song, P.-P., Fu, J.-J., Yue, Y.-H., 2016. Paleomagnetic constraints on the Mesozoic drift of the Lhasa terrane (Tibet) from Gondwana to Eurasia. Geology 44, 727–730. https://doi.org/10.1130/G38030.1.
Lippert, P.C., Zhao, X.-X., Coe, R.S., Lo, C.-H., 2011. Palaeomagnetism and $^{40}Ar/^{39}Ar$ geochronology of upper Paleogene volcanic rocks from Central Tibet: implications for the Central Asia inclination anomaly, the palaeolatitude of Tibet, and post-50 Ma shortening within Asia. Geophys. J. Int. 184, 131–161. https://doi.org/10.1111/j.1365-246X.2010.04833.x.
Liu, D., Zhao, Z.-D., Zhu, D.-C., Wang, Q., Sui, Q.-L., Liu, Y.-S., Hu, Z.-C., Mo, X.-X., 2011. The petrogenesis of postcollisional potassic-ultrapotassic rocks in Xungba basin, western Lhasa terrane: constraints from zircon U-Pb geochronology and geochemistry. Acta Petrol. Sin. 27 (7), 2045–2059.
Mattei, M., Muttoni, G., Cifelli, F., 2014. A record of the Jurassic massive plate shift from the Garedu Formation of central Iran. Geology 42 (6), 555–558.
Müller, R.D., Cannon, J., Qin, X., Watson, R.J., Gurnis, M., Williams, S., Pfaffelmoser, T., Seton, M., Russell, S.H., Zahirovic, S., 2018. GPlates: building a virtual Earth through deep time. Geochem. Geophys. Geosyst. 19 (7), 2243–2261.
Muttoni, G., Erba, E., Kent, D.V., Bachtadse, V., 2005. Mesozoic Alpine facies deposition as a result of past latitudinal plate motion. Nature 434 (7029), 59–63. https://doi.org/10.1038/nature03378.
Muttoni, G., Kent, D.V., 2019. Jurassic monster polar shift confirmed by sequential paleopoles from Adria, promontory of Africa. J. Geophys. Res., Solid Earth 124, 1–19. https://doi.org/10.1029/2018JB017199.
Oncken, O., Hindle, D., Kley, J., Elger, K., Victor, P., Schemmann, K., 2006. Deformation of the central Andean upper plate system - facts, fiction, and constraints for plateau models. In: The Andes. Springer, pp. 3–27.
Parsons, A.J., Sigloch, K., Hosseini, K., 2021. Australian plate subduction is responsible for northward motion of the India-Asia collision zone and ∼1000 km lateral migration of the Indian slab. Geophys. Res. Lett. e2021GL094904. https://doi.org/10.1029/2021GL094904.
Roberts, A.P., Almeida, T.P., Church, N.S., et al., 2017. Resolving the origin of pseudo-single domain magnetic behavior. J. Geophys. Res., Solid Earth 122, 9534–9558. https://doi.org/10.1002/2017JB014860.
Schepers, G., van Hinsbergen, D.J.J., Spakman, W., Kosters, M.E., Boschman, L.M., McQuarrie, N., 2017. South-American plate advance and forced Andean trench retreat as drivers for transient flat subduction episodes. Nat. Commun. 8 (15249), 1–9. https://doi.org/10.1038/ncomms15249.
Steinberger, B., Torsvik, T.H., 2008. Absolute plate motions and true polar wander in the absence of hotspot tracks. Nature 452 (7187), 620–623.
Steinberger, B., Torsvik, T.H., 2010. Toward an explanation for the present and past locations of the poles. Geochem. Geophys. Geosyst. 11 (6), 1–19. https://doi.org/10.1029/2009GC002889.
Tauxe, L., 2010. Essentials of Paleomagnetism. Univ. of California Press.
Tauxe, L., Shaar, R., Jonestrask, L., Swanson-Hysell, N., Minnett, R., Koppers, A., et al., 2016. PmagPy: software package for paleomagnetic data analysis and a bridge to the Magnetics Information cOnsortium (MagIC) Database. Geochem. Geophys. Geosyst. 17, 2450–2463. https://doi.org/10.1002/2016GC006307.
Tauxe, L., Mullender, T.A.T., Pick, T., 1996. Potbellies, wasp-waists, and superparamgnetism in magnetic hysteresis. J. Geophys. Res., Solid Earth 101 (B1), 571–583.
Tauxe, L., Watson, G.S., 1994. The fold test: an eigen analysis approach. Earth Planet. Sci. Lett. 122, 331–341.
Torsvik, T.H., Müller, R.D., Voo, R.V., Steinberger, B., Gaina, C., 2008. Global plate motion frames: toward a unified model. Rev. Geophys. 46 (RG3004), 1–44. https://doi.org/10.1029/2007RG000227.
Torsvik, T.H., Cocks, L.R.M., 2009. The Lower Palaeozoic palaeogeographical evolution of the northeastern and eastern peri-Gondwanan margin from Turkey to New Zealand. Geol. Soc. (Lond.) Spec. Publ. 325 (1), 3–21. https://doi.org/10.1144/SP325.2.
Torsvik, T.H., Van der Voo, R., Preeden, U., Niocaill, C.M., Steinberger, B., Doubrovine, P.V., van Hinsbergen, D.J.J., Domeier, M., Gaina, C., Tohver, E., Meert, J.G., McCausland, P.J.A., Cocks, L.R.M., 2012. Phanerozoic polar wander, palaeogeography and dynamics. Earth-Sci. Rev. 114 (3–4), 325–368.
Torsvik, T.H., van der Voo, R., Doubrovine, P.V., Burke, K., Steinberger, B., Ashwal, L.D., Tronnes, R.G., Webb, S.J., Bull, A.L., 2014. Deep mantle structure as a reference frame for movements in and on the Earth. Proc. Natl. Acad. Sci. USA 111 (24), 8735–8740. https://doi.org/10.1073/pnas.1318135111.
Vaes, B., van Hinsbergen, D.J., Boschman, L.M., 2019. Reconstruction of subduction and back-arc spreading in the NW Pacific and Aleutian Basin: clues to causes of Cretaceous and Eocene plate reorganizations. Tectonics 38 (4), 1367–1413.
Vaes, B., Li, S.-H., Langereis, C.G., van Hinsbergen, D.J.J., 2021. Reliability of palaeomagnetic poles from sedimentary rocks. Geophys. J. Int. 225 (2), 1281–1303. https://doi.org/10.1093/gji/ggab016.
van de Lagemaat, S.H., van Hinsbergen, D.J., Boschman, L.M., Kamp, P.J., Spakman, W., 2018. Southwest Pacific absolute plate kinematic reconstruction reveals major Cenozoic Tonga-Kermadec slab dragging. Tectonics 37 (8), 2647–2674.
van Hinsbergen, D.J.J., Schouten, T.L.A., 2021. Deciphering paleogeography from orogenic architecture: constructing orogens in a future supercontinent as thought experiment. Am. J. Sci. 321, 955–1031.
Yi, Z.-Y., Liu, Y.-Q., Meert, J.G., 2019. A true polar wander trigger for the great Jurassic East Asian Aridification. Geology 47, 1112–1116. https://doi.org/10.1130/G46641.1.
Zheng, M., Song, Y., Li, H., Guilmette, C., Tang, J., Zhang, Q., Liu, Z., Li, F., 2022. Triassic trachytic volcanism in the Bangong–Nujiang Ocean: geochemical and geochronological constraints on a continental rifting event. Geol. Mag. 159, 519–534.
Zhu, D.-C., Zhao, Z.-D., Niu, Y., Mo, X.-X., Chung, S.-L., Hou, Z.-Q., Wang, L.-Q., Wu, F.-Y., 2011. The Lhasa terrane: record of a microcontinent and its histories of drift and growth. Earth Planet. Sci. Lett. 301, 241–255. https://doi.org/10.1016/j.epsl.2010.11.005.
Zhu, D.-C., Zhao, Z.-D., Niu, Y., Dilek, Y., Hou, Z.-Q., Mo, X.-X., 2013. The origin and pre-Cenozoic evolution of the Tibetan Plateau. Gondwana Res. 23 (4), 1429–1454. https://doi.org/10.1016/j.gr.2012.02.002.
Zhu, Z.-W., 1985. Comparative significance of apparent polar wander path of Xizang and its adjacent regions from Phanerozoic. Acta Geophys. Sin. 28 (Suppl. 1), 219–226.